



The effects of Ag content and dendrite spacing on the electrochemical behavior of Pb–Ag alloys for Pb-acid battery components



Wislei R. Osório^{a,b,*}, Leandro C. Peixoto^b, Amauri Garcia^b

^a School of Applied Sciences – FCA, University of Campinas – UNICAMP, Campus Limeira, 1300, Pedro Zaccaria St., Jd. Sta Luiza, 13484-350 Limeira – SP, Brazil

^b Department of Materials Engineering, University of Campinas – UNICAMP, PO Box 6122, 13083-970 Campinas – SP, Brazil

HIGHLIGHTS

- Dendritic array and Ag content affect corrosion behavior of Pb–Ag alloys.
- The role of microstructure on the corrosion current density is more significant.
- Pb–Ag alloys are qualified as alternative materials for lead-acid battery components.

ARTICLE INFO

Article history:

Received 5 January 2013

Received in revised form

12 February 2013

Accepted 5 March 2013

Available online 26 March 2013

Keywords:

Pb–Ag alloys

Dendrite spacings

EIS

Polarization

Equivalent circuit

ABSTRACT

The present study proposes correlations between the silver content and the dendrite arm spacing of two distinct Pb–Ag alloys (1 and 2.4 wt.% Ag) with their resulting electrochemical corrosion responses. Samples having a wide range of dendritic spacings were obtained using a water-cooled unidirectional solidification system. EIS, potentiodynamic polarization curves and an equivalent circuit were used to characterize the corrosion behavior of these samples in a 0.5 M H₂SO₄ solution at 25 °C. It was found that both the Ag alloying and the scale of secondary dendritic arm, λ_2 , have important roles on the electrochemical corrosion behavior. The current density decreased with the increase in λ_2 . The increase in silver content provoked only a slightly improvement in the corrosion resistance and its addition to a Pb alloy should meticulously be analyzed considering the ratio anode/cathode areas. Although the addition of silver increases considerably the final cost of Pb–Ag alloys, these alloys can be used as alternative materials for the manufacture of lead-acid battery components.

© 2013 Elsevier B.V. All rights reserved.

1. Introduction

In the manufacture of components for Pb-acid batteries (positive and negative grids, connectors, etc), the producers commonly use Pb–Sb, Pb–Sn and Pb–Sn–Ca alloys [1–4]. Particularly, these alloys have been widely used in the production of positive grids of valve regulated lead-acid (VRLA) batteries. It is known [4–7] that the charge–discharge performance of a Pb-acid battery can be significantly improved with the addition of antimony. However, this enhances gas evolution (hydrogen) leading to excessive water consumption from the H₂SO₄ electrolyte and increasing self-

discharge. Besides, a Pb–Sn–Ca alloy is considerably more susceptible to severe deterioration at high temperature under charge–discharge cycles [8–10].

In order to assess the performance of Pb-based alloys used for lead-acid battery components, a number of experimental investigations have been carried out. Zhou et al. [10] and Liu et al. [11] reported an increase in the corrosion resistance at a deep discharge cycle (0.9 V vs. Hg/Hg₂SO₄) [10] and a decrease in the resistance of the anodic Pb (II) oxide film with Sm and Ce (RE – rare earth) additions. Bashtavelova and Winsel [12] have reported that the addition of tellurium improves the mechanical behavior, anti-corrosive ability and performance under charge–discharge cycles. Guo et al. [13] investigated different Pb–Te alloys (0.01–1.0 wt.% Te) and reported that the Te alloying induced a microstructural grain refinement, which increased the corrosion resistance. Electrochemical impedance results (Nyquist plots) revealed

* Corresponding author. School of Applied Sciences – FCA, University of Campinas – UNICAMP, Campus Limeira, 1300, Pedro Zaccaria St., Jd. Sta Luiza, 13484-350 Limeira – SP, Brazil.

E-mail address: wislei.osorio@fca.unicamp.br (W.R. Osório).

that the resistance to the corrosion reaction (formation of PbO_2) on the electrode surface increased with the Te content of the alloy [13]. These authors have also suggested that Te inhibits the growth of PbO_2 .

Considering the silver addition to a Pb–Ca–Sn alloy, Prengaman [4] reported that Ag increases both the corrosion and creep resistances, improving considerably grid processing and battery performance and durability at high temperature service.

Pb–Ag binary alloys are used as anodes in most of zinc electrowinning industries [13,14]. Due to their high corrosion resistance, high electrochemical activity, anode working life, energy consumption and production costs these Pb–Ag alloys are considered good materials of choice for anodes [13]. These Pb–Ag alloys have lower overpotential for anode reaction when compared with other anode materials. Besides, other aspects can also be considered with respect to silver content. Although the refining of secondary lead is not as complex as refining of primary lead, some low levels of silver (and commonly bismuth) are below of the required specification limits for most Pb alloys and do not require removal [15]. The major removal steps for Cu, Ni and other elements are carried out [15]. Moreover, silver contamination can have serious effects on performance of active materials due to the oxygen reduction overpotential [16].

Although some investigations have focused on the use of Pb-based multicomponent alloys for battery parts, the control of the as-cast microstructure array of binary alloys can be an alternative way for the manufacture of lead-acid battery components with better electrochemical behavior, as previously reported for Pb–Sb and Pb–Sn alloys, [7,17–24].

It is known that different resulting microstructures are generated as a function of a variety of grid manufacturing processes. A series of experimental studies [17–24] reported that Pb-based binary alloys having coarser cellular array tend to have higher corrosion resistance than finer cellular arrangements, and that this is associated with the reduction in cellular boundaries. On the other hand, for dendritic microstructures, finer dendritic arm spacings improve the electrochemical corrosion response of a Pb-based binary alloy [23,24], which is intimately correlated with a more homogeneous distribution of the anodic Pb-rich phase throughout the microstructure.

The aim of this investigation is to assess the effect of two different silver contents (1 and 2.5 wt.% Ag), on the resulting microstructure array and on the electrochemical behavior of Pb–Ag alloys. A water-cooled directional solidification apparatus was used to obtain samples, along the casting length, having a wide range of dendritic arm spacings permitting a comparative analysis to be carried out.

2. Experimental procedure

2.1. Specimens and solidification setup

In order to prepare the Pb–1 wt.% Ag and Pb–2.4 wt.% Ag alloys, commercially pure (c.p.) metals Pb (99.91 wt.%) and Ag (99.99 wt.%) were used. An X-ray fluorescence technique was used to determine the chemical concentrations (Rigaku® Rix 3100). For this, an area of 100 mm² was considered in three distinct specimens of each metal. The impurity percentages detected in Ag and Pb were: Sn (0.001 wt.%), Pb (0.0027 wt.%); and Sn (0.0115 wt.%), Fe (0.08 wt.%), Si (0.001 wt.%), respectively, besides other minor elements less than 150 ppm.

Fig. 1 depicts the typical solidification set-up used to obtain directionally solidified castings of the Pb–Ag alloys examined. This solidification apparatus promotes upward directional solidification with heat flow extracted only through the water-cooled bottom

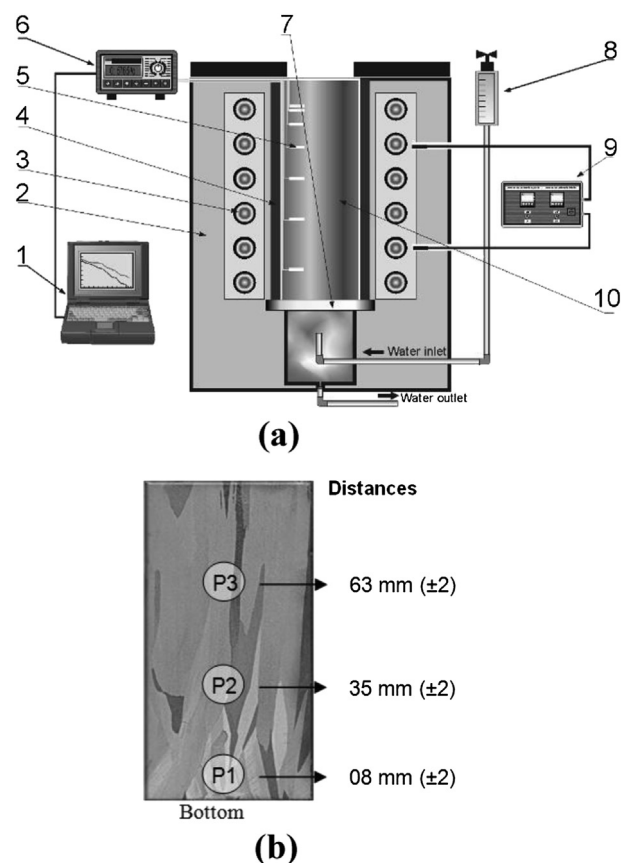


Fig. 1. (a) Experimental solidification set-up: 1) computer and data acquisition software; 2) insulating ceramic shielding; 3) electric heaters; 4) mold; 5) thermocouples; 6) data logger; 7) heat-extracting bottom; 8) water-flow meter; 9) temperature controller; 10) casting; and (b) schematic representation of a macrostructure depicting three distinct positions in casting from where the samples for corrosion tests were extracted.

(cylindrical stainless steel mold: 50 mm × 110 mm and wall-thickness of 3 mm), as previously reported [17–24].

A solution of 37.5 mL of glacial acetic acid and 15 mL of H_2O_2 , at 25 °C was used to reveal the microstructure. An image processing system Neophot 32 (Carl Zeiss®) and Leica-500® (Quantimet 500 MC) was used as to measure the secondary dendritic arm spacing, λ_2 . For each selected specimen, about 20 measurements of λ_2 were taken at longitudinal sections. A scanning electron microscope, SEM (Jeol® model JXA 840A) and an energy dispersive X-ray detector (EDAX, Noran) were also used for microstructural characterization. For each selected region, at least five SEM backscattered electron images were used for microstructural characterization and chemical analysis.

2.2. EIS and potentiodynamic polarization measurements

Selected samples collected at different positions along the casting length were subjected to EIS and potentiodynamic polarization tests, as shown in Fig. 1. Firstly the EIS measurements were carried out followed by the potentiodynamic polarization, which were conducted in a stagnant and naturally aerated 500 cm³ solution of H_2SO_4 having a concentration of 0.5 mol L⁻¹ (0.5 M) at 25 °C. All electrochemical corrosion experiments were performed in a 1 cm² circular area of ground (1200 grit SiC finish) alloy samples. All experiments were carried out in a stagnant and naturally aerated solution to simulate the battery electrolytic fluid under pH of about 0.92 (± 0.16). EIS tests were conducted with a potentiostat

(EG&G Princeton Applied Research®) coupled to a frequency analyzer system (Solartron®). A glass corrosion cell-kit containing the working electrode (Pb–Ag alloy sample), a platinum counter-electrode and a saturated calomel reference electrode (SCE) were also used to carry out the EIS experiments. It is important to remark that the electrochemical behavior of Pb–acid battery systems is commonly evaluated using a MSE electrode (MSE – Mercury/Mercurous Sulfate Electrode or Hg/Hg₂SO₄ or similar). Although a SCE electrode is not commonly used in Pb–acid system studies, the one inconvenient is the fact that chloride may slightly contaminate the electrolyte, another SO₄^{2−} may also contaminate the electrode decreasing its working-life inducing repetitive verification and calibration. At open-circuit, a 10 mV of the potential amplitude was set in a peak-to-peak signal and the frequency range was set from 100 mHz to 100 kHz resulting in five points per decade.

The EIS tests were carried out at the same selected positions where the potentiodynamic measurements were performed. A 0.5 M H₂SO₄ solution at 25 °C was also used to carry out the polarization tests using the aforementioned potentiostat. A scan rate of 0.1667 mV s^{−1} was selected in order to conduct these tests by stepping the potential at open-circuit. From the Tafel plots, both the corrosion current density and corrosion potential were determined by using the cathodic/anodic branches at a scan rate of 0.1667 mV s^{−1} from −250 mV (SCE) to +250 mV (SCE) at open-circuit. This mentioned potentiodynamic range corresponds to −600 mV to −150 mV (MSE). Duplicate tests for both the EIS and potentiodynamic polarization curves were carried out. In order to provide quantitative impedance parameters, such as polarization resistances and capacitances, an appropriate model (ZView version 2.1b) for equivalent circuit quantification was also used, permitting simulated and experimental results to be compared.

3. Results and discussion

3.1. Dendrite arm spacings and cooling rate

Samples for the electrochemical investigations were extracted from selected positions along the castings lengths: P1 = 8 (±2) mm, P2 = 35 (±2) mm and P3 = 63 (±2) mm, as shown in Fig. 1(b). These positions were selected with a view to permitting samples having quite different secondary dendrite arm spacings (λ_2) to be compared in terms of their electrochemical properties (e.g. current densities and polarization resistances).

Fig. 2(a) depicts the experimental results of λ_2 with the position from the cooled surface of the castings for each alloy examined. The solidification cooling rate is high close to the cooled bottom decreasing toward the top of the casting, due to the increasing thermal resistance of the solid formed. Fig. 2(b) shows the evolution of λ_2 as a function of the cooling rate (dT/dt) for both the Pb–1 wt.% Ag and Pb–2.4 wt.% Ag alloys castings. As expected, λ_2 is smaller for positions close to the cooled surface and increase with the increase in distance from the bottom of the casting. This is intimately associated with the resulting cooling rate, as similarly observed in previous investigations [17–24].

Typical microstructural arrays observed on longitudinal sections of the Pb–1 wt.% Ag and Pb–2.4 wt.% Ag alloys castings are shown in Fig. 3. Due to higher cooling rates near the casting/chill surface λ_2 is smaller (± 5 μ m and 8 μ m for Pb–1 and Pb–2.4 wt.% Ag alloys, respectively) close to the bottom of the casting and larger (± 50 μ m) for positions far from it. It is also interesting to observe that tertiary dendrite arm spacings (λ_3) were found at positions 37 mm and 65 mm of the Pb–2.4 wt.% Ag alloy casting, which correspond to cooling rates lower than 2 °C s^{−1}.

The microstructures of these Pb–Ag alloys are constituted by a Pb-rich matrix having a dendritic morphology (α -phase: solid

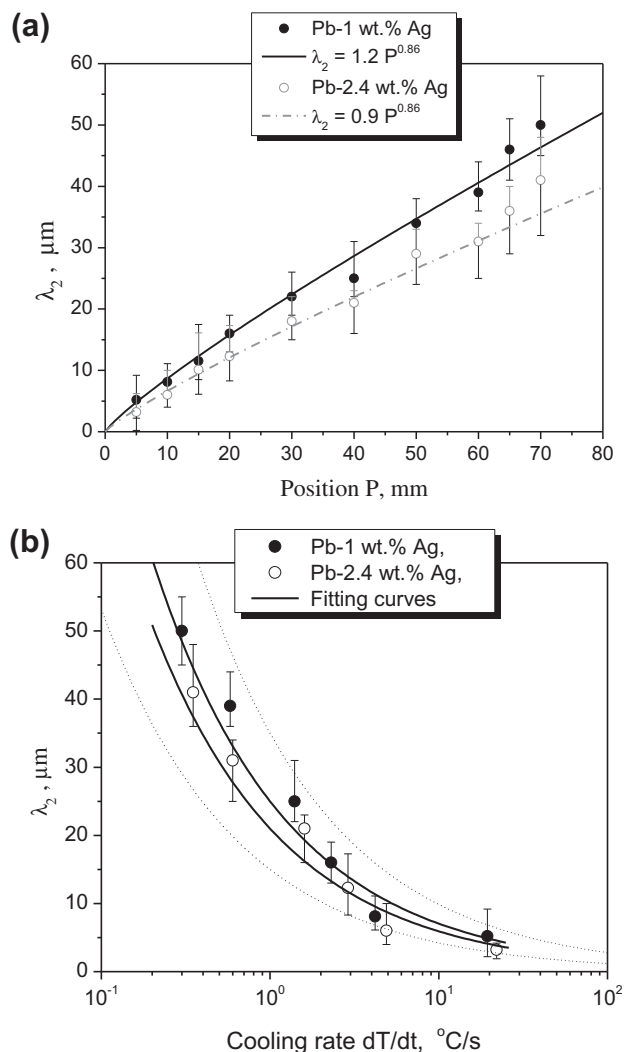


Fig. 2. Evolution of secondary dendritic arm spacings (λ_2) with (a) the position (distance) from the bottom of casting; and (b) with the cooling rate (dT/dt) for the examined Pb–Ag alloys samples.

solution of silver in lead, light region) with a predominantly lamellar eutectic mixture (eutectic composition: 2.5 wt.% Ag) into the inter-dendritic regions (dark region). A complete Pb–Ag phase diagram with details between 0 and 0.15 wt.% Ag and a partial phase-diagram (from 0 to 10 wt.% Ag) are shown in Fig. 4(a) and (b), respectively.

Considering the phase diagram, the equilibrium partition coefficient (k) can be calculated at the eutectic temperature (304 °C), by:

$$k = C_S / C_L \quad (1)$$

where C_S and C_L are the solid and liquid compositions at the eutectic temperature (solubility limit and eutectic compositions, respectively). Thus, C_S is 0.1 and C_L is 2.5 resulting in $k = 0.04$. In order to estimate the eutectic fraction (f_E) of each Pb–Ag alloy examined, the parameter (k) is introduced into Scheil's equation [25]. Thus, the calculated f_E formed during the non-equilibrium solidification for Pb–1 wt.% Ag and Pb–2.4 wt.% alloys are $f_E = 38.5\%$ and $f_E = 95.8\%$, respectively.

Fig. 4(c) depicts a typical cooling curve of a Pb–1 wt.% Ag alloy which was slowly cooled (close to equilibrium solidification) evidencing the liquidus (317 °C) and eutectic (304 °C) temperatures, as also indicated in the partial phase diagram of Fig. 4(b).

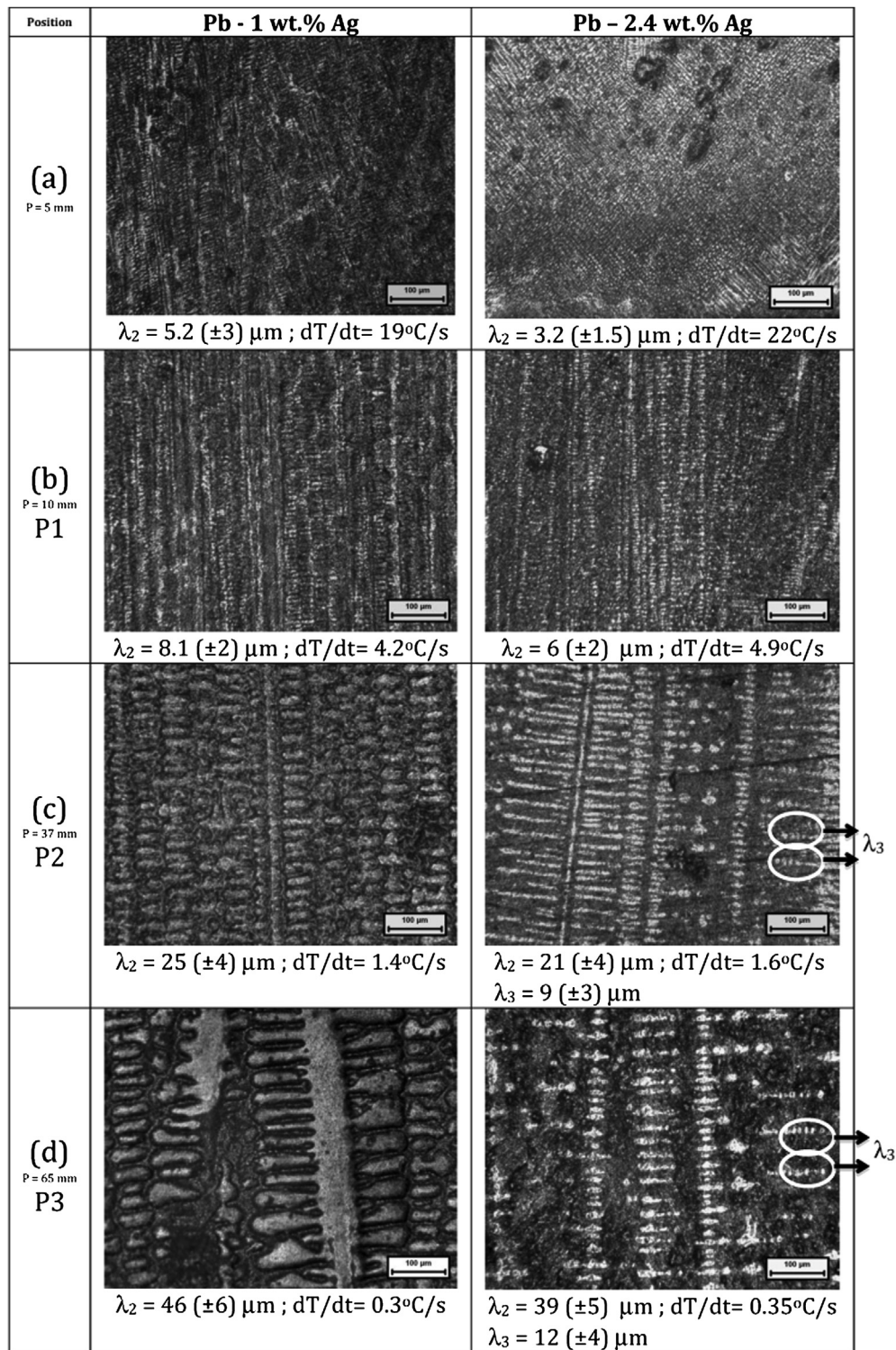


Fig. 3. Typical longitudinal microstructures along the Pb-1 wt.% Ag and Pb-2.4 wt.% Ag alloys castings at: (a) 5 mm, (b) 10 mm (position: P1), (c) 37 mm (position: P2) and (d) 65 mm (position P3) from the bottom of the casting.

During non-equilibrium solidification, the α Pb-rich phase will have an increasingly silver content from the center of the dendrite core toward the interdendritic region, up to a eutectic concentration (2.5 wt.% Ag), as schematically shown in Fig. 5. According to Scheil's equation [25], the initial solid formed for a Pb-1 wt.% Ag alloy has 0.04 wt.% Ag and the solid composition increases up to 0.1 wt.% Ag (silver solubility limit) considering the dendritic matrix.

At the center of the interdendritic region the composition of silver will attain the eutectic composition i.e. 2.5 wt.% A. For the Pb-2.5 wt.% Ag alloy, the chemical composition of the Pb-rich matrix varies from 0.096 wt.% Ag up to 0.1 wt.% Ag, as shown in Fig. 5.

A typical SEM micrograph of a Pb-1 wt.% Ag alloy sample indicating the locations, where the EDAX analyses were carried out is shown in Fig. 6. The representative EDAX patterns (points #1 to #4)

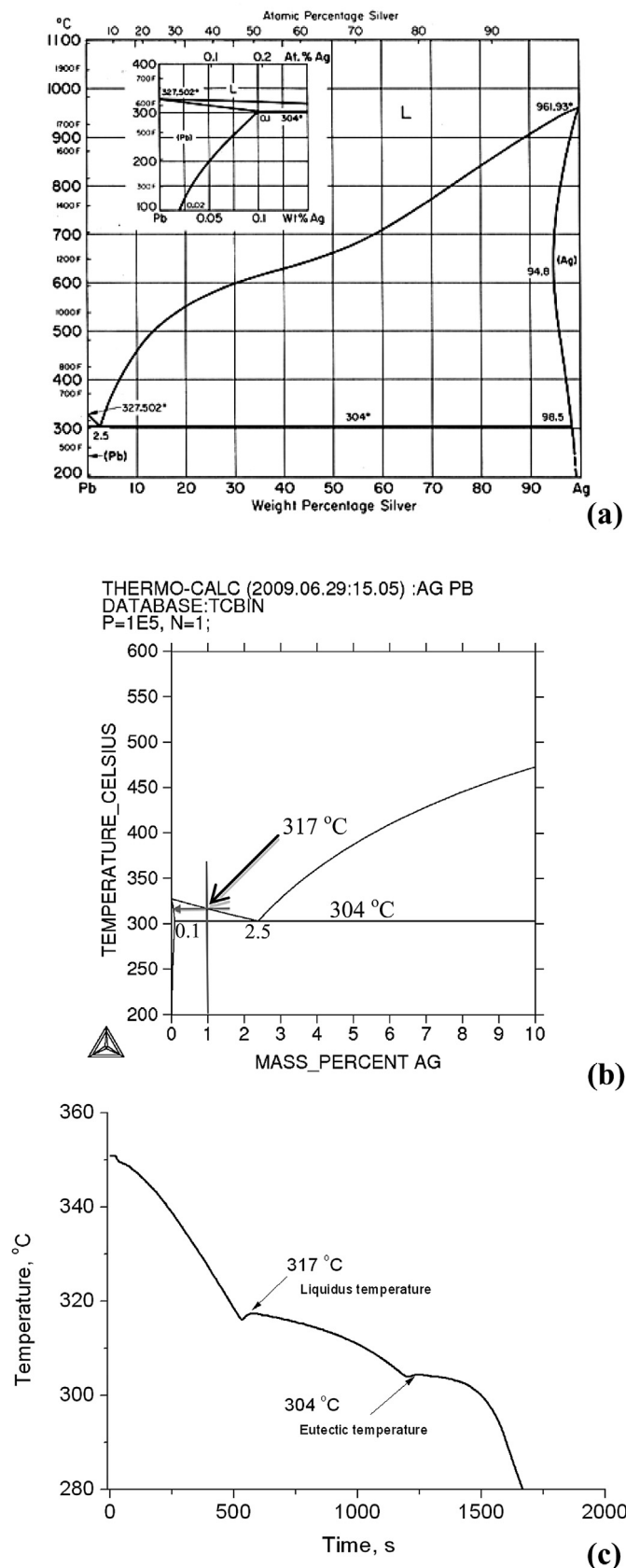


Fig. 4. (a) Complete and (b) partial Pb–Ag phase diagram and (c) a typical equilibrium cooling curve of a Pb–1 wt.% Ag alloy.

and the corresponding chemical analyses are also shown in Fig. 6. The eutectic mixture (points #1 and 2) in the interdendritic regions will commonly be formed by alternated Pb-rich and Ag-rich phases. The EDAX analysis reveals that points #1 and 2 have average compositions close to the eutectic concentration, i.e. 2.5 wt.% Ag. On the other hand, it can be seen that points #3 and #4 correspond to the Pb-rich dendritic matrix with concentrations close to those corresponding to that of the primary solid formed up to the Ag solubility limit (i.e. between 0.04 and 0.1 wt.% Ag).

Fig. 7 shows the experimental results of X-ray fluorescence carried out in order to determine the chemical concentrations along the alloys casting length. It can be seen that silver is fairly well distributed along the castings length having compositions quite close to the nominal compositions of the alloys examined, without any evidence of macrosegregation. Since silver and lead have similar densities (10.5 g cm^{-3} and 11.3 g cm^{-3} , respectively), gravity driven segregation was not expected.

3.2. EIS and equivalent circuit results

Figs. 8 and 9 show the Bode, Bode-phase and Nyquist plots obtained in a 0.5 M H_2SO_4 solution at room temperature for the Pb–1 wt.% Ag and Pb–2.4 wt.% Ag alloys, respectively, i.e. the modulus of impedance ($|Z|$) and phase angle (θ) as a function of frequency and $Z_{\text{Imaginary}}$ and Z_{Real} plots, respectively. A rapid observation of the Bode-phase plots of the Pb–1 wt.% Ag alloy, seems to indicate that only one time constant exists. On the other hand, when the Pb–2.4 wt.% Ag alloy is analyzed, two time constants can be seen. For the Bode-phase plots of the Pb–1 wt.% Ag alloy, particularly between 10^3 and 10^5 Hz, two time constants can also be considered. Besides, the fitting between simulated and experimental results will also indicate two time constants, as will be discussed further in this section. These time constants are associated with the corrosion kinetics of the Pb–Ag alloys samples, where at 10^4 – 10^5 Hz, a first time constant seems (more pronounceable in Pb–2.4 wt.% Ag alloy) to be related with the reaction between the electrolyte and the Ag-rich phase in the interdendritic region. This observation is more remarkable for the sample at position P1.

Considering the examined Bode plots there are three distinct regions: (i) at low frequencies between 10^{-2} and 10^0 Hz, which represent the polarization resistances of the alloy samples, the observed $|Z|$ measurements for the Pb–1 wt.% Ag and Pb–2.4 wt.% Ag alloys samples are between 200 and 400 $\Omega \text{ cm}^2$ and 200 and 600 $\Omega \text{ cm}^2$, respectively; (ii) at intermediate frequencies (between 10^0 and 10^4 Hz), the examined samples corresponding to P2 and P3 (i.e. 37 and 65 mm from the cooled surface) show similarities in both the electrochemical double layer characteristics and maximum phase angles (θ_{max}). However, the samples examined at positions P1 (10 mm from the cooled surface) of both the Pb–1 and Pb–2.4 wt.% Ag alloys, have shown distinct double layer characteristics when compared with those of positions P2 and P3. The Pb–1 wt.% Ag alloy evidences at 10 Hz a phase angle (θ) of about 55 degrees (first time constant) and a second time constant at about 2×10^4 Hz with θ of 30 degrees. For the Pb–2.4 wt.% Ag alloy, the 1st time constant occurs at 50 Hz with θ of about 20 degrees; and (iii) at the range of frequencies between 10^4 and 10^5 Hz, the values of $|Z|$ indicate an electrolyte resistance (about 4 Ω), which is very similar for both Pb–Ag alloys examined in this investigation.

The preceding discussions on the impedance characteristics give indications that, from all samples examined that with the smallest dendritic spacing (and consequently with more homogeneous distribution of the eutectic mixture throughout the microstructure: positions P1) can be associated with the best electrochemical behavior.

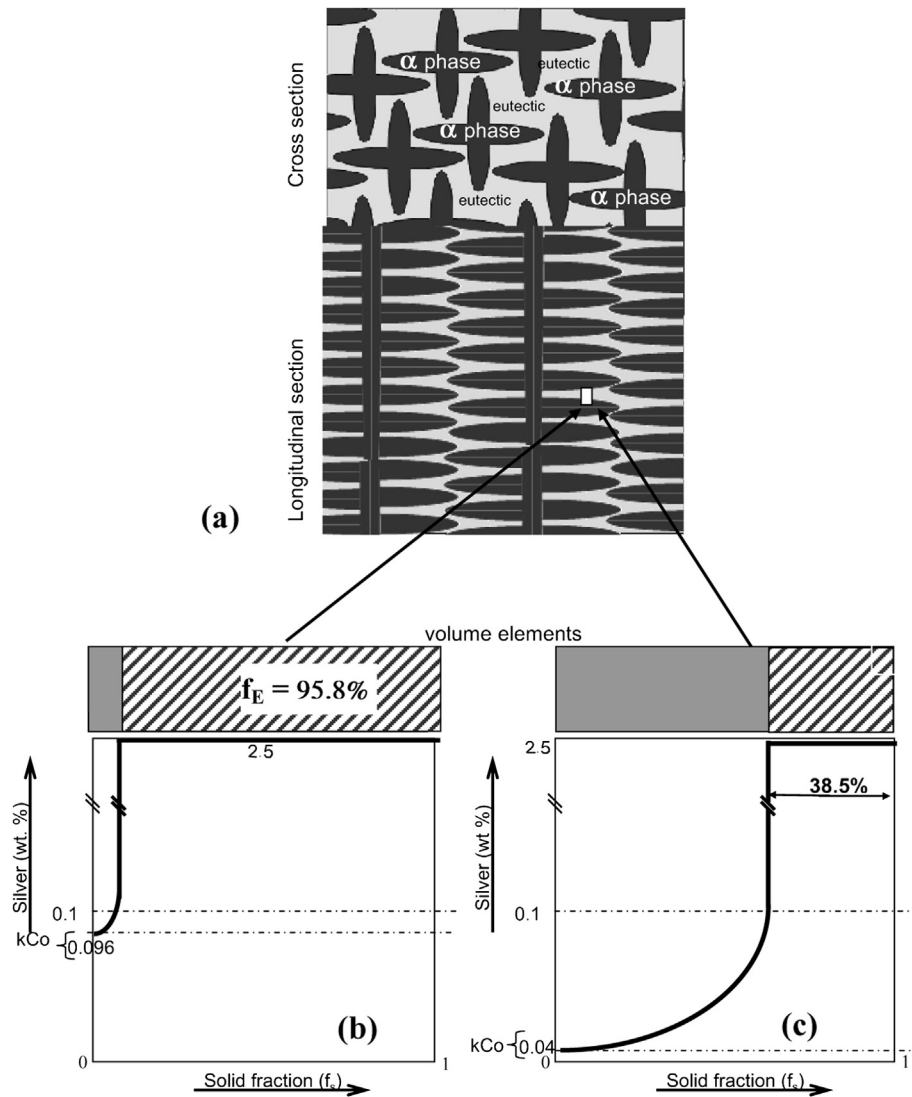


Fig. 5. (a) Schematic representation of a dendritic arrangement (cross and longitudinal sections) showing the variation of silver content along volume elements encompassing the dendritic matrix and interdendritic region for: (b) Pb-2.4 wt.% Ag and (c) Pb-1 wt.% Ag alloys.

Simulated and experimental results in Nyquist plots of all Pb–Ag alloys samples examined are shown in Figs. 8(b) and 9(b). All Nyquist plots are characterizing capacitive semi-arcs. The highest capacitive semi-arc is that of positions P1 (10 mm from the bottom of the casting) for both alloys. The examined positions P2 show intermediate capacitive semi-arcs followed by those corresponding to the positions P3. It is remarkable that these Nyquist plots do not show slopes of 45° at low frequencies (i.e. commonly between 0.3 and 0.01 Hz), as previously observed for Pb–Sn alloys with similar solute contents [19].

Another interesting observation is related to the magnitude of the observed semi-arcs, which is similar to that verified for both Pb–Sn [19] and Pb–Sb [22] alloys under similar cooling rate conditions, i.e. using the same water-cooled unidirectional solidification system.

Fig. 10 shows the equivalent circuit used to provide quantitative support to the aforementioned experimental EIS results, as similarly reported in previous studies [17–24]. With the proposed equivalent circuit the fitting between the experimental and simulated data was made. The impedance parameters obtained by the ZView® software and the chi-squared (χ^2) values, which are

associated with the fitting quality, are shown in Tables 1 and 2 for the Pb-1 wt.% Ag and Pb-2.4 wt.% Ag alloys, respectively.

Considering the interpretation of the physical elements of the proposed equivalent circuit, the parameters R_{el} denotes the electrolyte resistance, R_1 is the charge transfer resistance and R_2 stands for a polarization resistance due to the participation of adsorbed intermediates (e.g. HSO_4^- , H^+ and OH^- ions).

For simplicity, a constant-phase element representing a shift from an ideal capacitor was used instead of the capacitance itself. The $Z_{CPE(1)}$ and $Z_{CPE(2)}$ designate the double layer capacitance linked with the charge transfer resistance (R_1) and the capacitance, which is associated with the polarization resistance R_2 , respectively. Varying between -1 and 1 the parameters n_1 and n_2 are intimately correlated with the corresponding phase angles. Besides, they can also be associated with the non-uniform distribution of current as a result of surface defects or roughness [21–24]. It can also be said that Z_{CPE} denotes the impedance of a constant phase element and can be expressed by [17–24]:

$$Z_{CPE} = [C(j\omega)^{n_1}]^{-1} \quad (2)$$

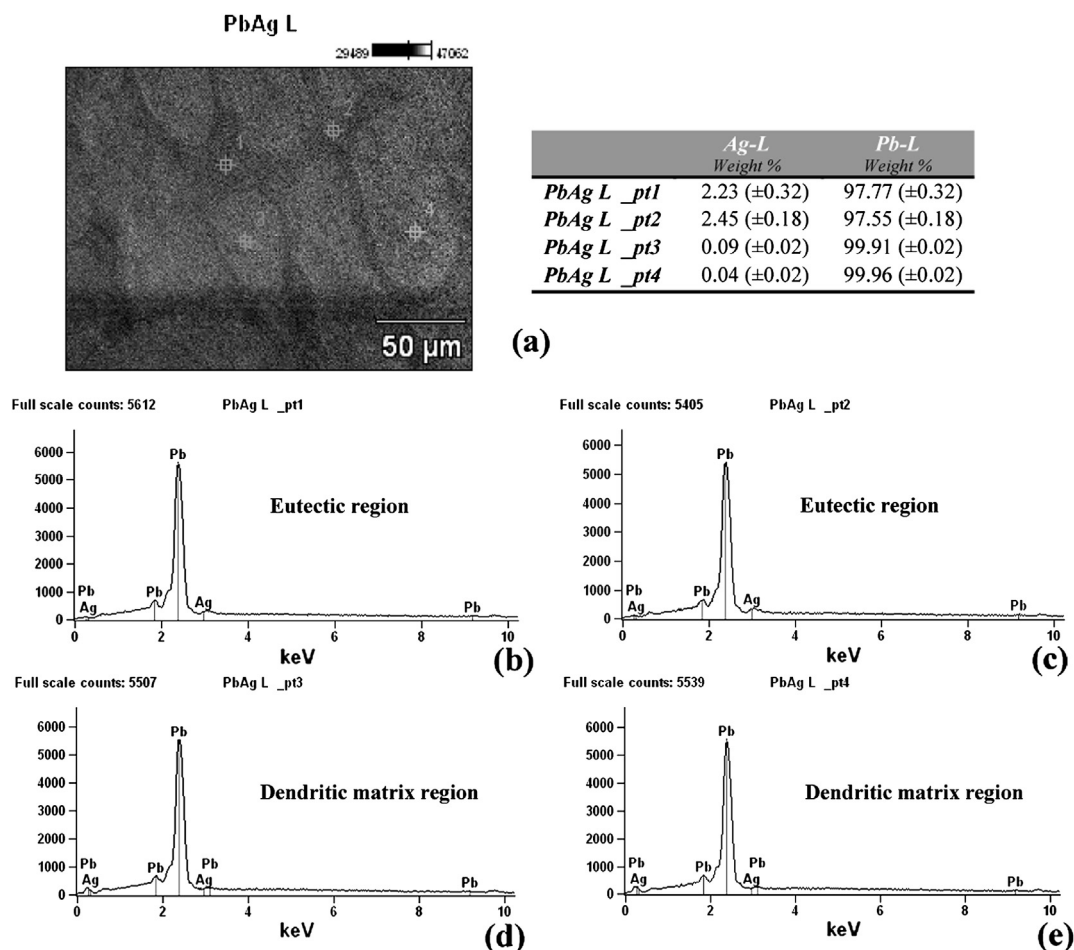


Fig. 6. (a) Typical SEM image for a Pb–Ag alloy and table with indicated local composition of each element at different points of the microstructure obtained by EDAX analysis (b–e).

where C is the capacitance; j is the current; ω is the frequency and $-1 \leq n \leq 1$.

Tables 1 and 2 show that the double layer capacitances ($Z_{CPE(1)}$) are lowest for positions P1 associated with values of the charge

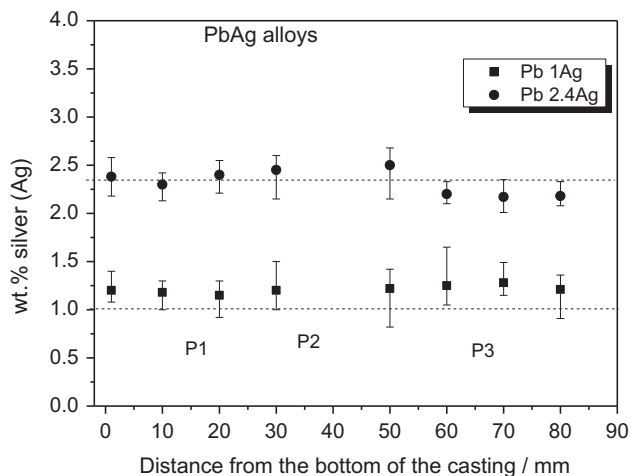


Fig. 7. (a) Experimental Ag concentration profile along the casting length of the two Pb–Ag alloys examined.

transfer resistance (R_1). It is known that low capacitances are intimately associated with an increase in the thickness of the passive layer [26,27]. It is very important to remember that the capacitances Z_{CPE} should be analyzed and associated with their corresponding polarization resistances. Since R_1 is commonly lower than R_2 and R_1 and R_2 denote the charge transfer and polarization resistances, respectively, it can be observed that the position P1, which is closest to the bottom of the casting, has higher resistance than positions P2 and P3 for both alloys examined. Thus, the Pb-1 wt.% Ag alloy shows R_2 decreasing from P1 to P3. The position P1 has ($R_1 + R_2$) about 60% and 66% higher than positions P2 and P3, respectively. For the Pb-2.4 wt.% Ag alloy, the position P1 shows ($R_1 + R_2$) about 3.5 times higher than P2 and P3. It can be observed that the position P1 for the Pb-2.4 wt.% Ag alloy has ($R_1 + R_2$) about 57% higher (551 against $344 \Omega \text{ cm}^2$) than the more dilute alloy (1 wt.% silver).

Comparing these values of polarization resistances with those previously obtained for Pb–Sb and Pb–Sn alloys [20,24], it can be seen that they are similar to those of the Pb–Sb alloys. It should also be mentioned that for the Pb-1 wt.% Ag alloy, R_1 decreases from position P1 to P3, i.e., 344, 121 and $84 \Omega \text{ cm}^2$. These values are correlated with the charge transfer resistances of these alloy samples. On the other hand, the Pb-2.4 wt.% Ag alloy samples evidence the polarization resistance (R_2), which is associated with absorbed intermediate species, higher than R_1 . Thus, it seems that the electrochemical behavior of a dilute Pb-1 wt.% Ag alloy is

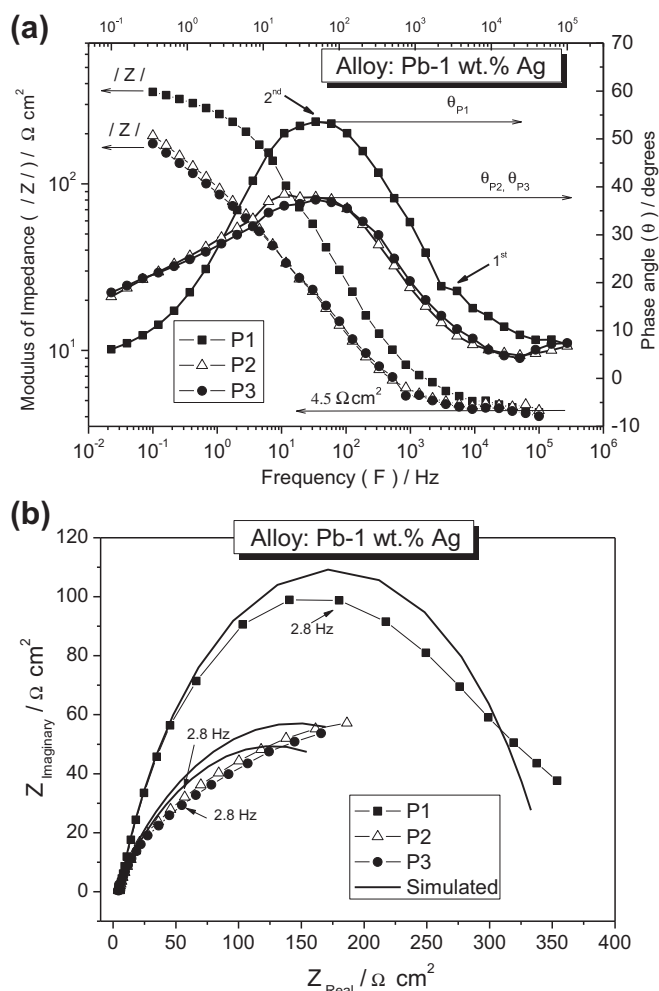


Fig. 8. Experimental results for the Pb-1 wt.% Ag alloy samples in a 0.5 M H₂SO₄ solution at 25 °C: (a) Bode and Bode-phase and (b) experimental and simulated Nyquist plots.

predominantly guided for R_1 (charge transfer resistance) and in the case of the Pb-2.4 wt.% Ag alloy, R_2 guides the electrochemical kinetics (involving intermediate adsorbed species, as HSO_4^- , H^+ or OH^- ions). Adsorption of both HSO_4^- and OH^- ions can occur simultaneously at the surface of the working electrode (electrolyte/sample) interface, while H^+ ions into cracks or cavities of oxide or corrosion by products. This can cause variation in the charge transfer (Helmholtz electrochemical double layer). These adsorbed species can significantly stimulate the dissolution of the metal, which can be drastically increased or minimized depending on the nature and characteristics of the corrosion product formed.

Comparing the abovementioned values of polarization resistances with those previously determined for Pb–Sn alloys [20], it can be seen that Pb–Sn alloys have higher values due to their higher tendency to oxide film formation, which can be associated with higher corrosion current densities. However, based only on these results it is not possible to conclude that the Pb–Sn alloys have better electrochemical corrosion behavior than the Pb–Ag alloys, since both the EIS (capacitances and resistances) and potentiodynamic polarization parameters (corrosion potential and current density) must also be simultaneously analyzed. In this sense, in next section the experimental parameters of polarization plots will be discussed.

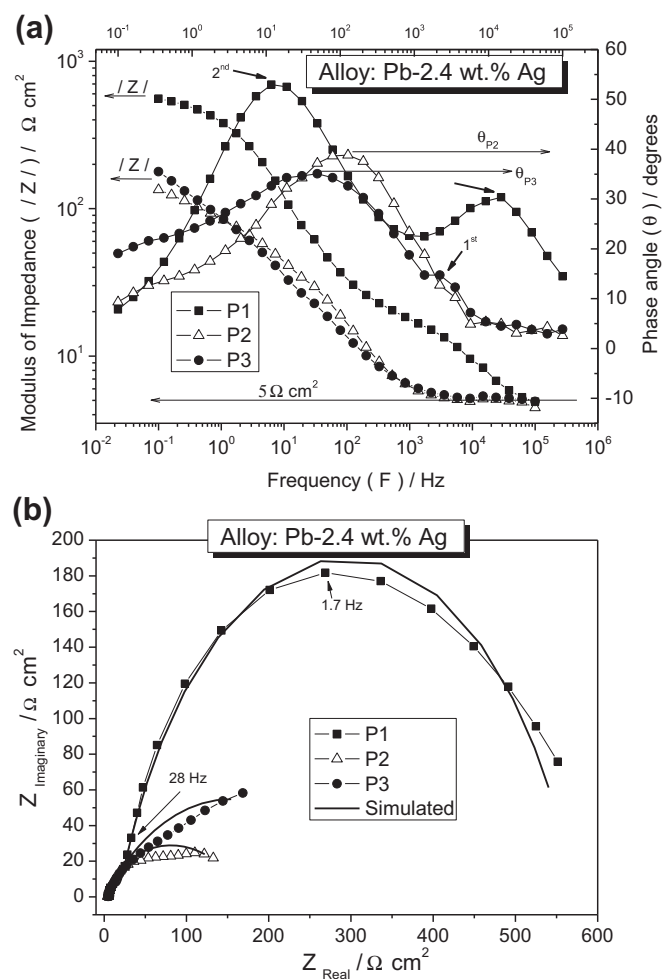


Fig. 9. Experimental results for the Pb-2.4 wt.% Ag alloy samples in a 0.5 M H₂SO₄ solution at 25 °C: (a) Bode and Bode-phase and (b) experimental and simulated Nyquist plots.

3.3. Potentiodynamic polarization results with EIS and microstructural array

Fig. 11 presents the potentiodynamic polarization curves between –425, –450 and –600 mV (SCE) for the Pb–Ag alloys samples at three different positions (P1, P2 and P3) carried out in a 0.5 M H₂SO₄ solution at 25 °C. Both the cathodic and anodic branches were considered in Tafel plots in order to obtain the experimental current density (i_{corr}). These i_{corr} values associated with the previously discussed EIS parameters reinforce the assertion that a better electrochemical corrosion behavior is associated with samples from positions P1, decreasing sequentially up to P3.

A corrosion current density of $10.3 (\pm 1.3) \mu\text{A cm}^{-2}$ was attained for the Pb-1 wt.% Ag alloy sample at the position P1. This i_{corr} increases with the increase in distance from the cooled surface of the casting, i.e. about 30 and $45 \mu\text{A cm}^{-2}$ for the positions P2 and P3, respectively. For the Pb-2.4 wt.% Ag alloy, the sample at position P1 attains an i_{corr} of $6.8 (\pm 2.5) \mu\text{A cm}^{-2}$ while P2 and P3 have i_{corr} about 4 and 6 times higher than that of P1, respectively.

In all examined polarization plots along a range of potentials from –600 and –425 mV (SCE), it can be said that the current depends on the spot the sample was taken. However, at more positive potentials this practically disappears and the samples depict similar electrode systems, i.e. Pb/PbO/PbSO₄ and Pb/PbO₂, as

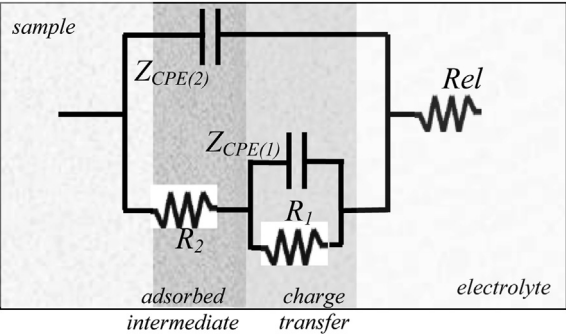


Fig. 10. Proposed equivalent circuit used to simulate and obtain impedance parameters.

also previously reported for Pb–Sn alloys [19,20,24]. Before the formation of PbO/PbSO₄ and PbO/PbO₂ as electrode systems, the scale of the dendrite spacing conducts the corrosion kinetics, and after this the electrochemical behavior will be very similar and connected to the oxide layer growth when the stability of the electrode systems is attained (usually in the range +400 mV to +1500 mV, SCE) [19,20,24].

A comparison between the experimental values of current density (i_{corr}) as a function of the secondary dendrite arm spacings (λ_2) for the Pb–1 wt% Ag and Pb–2.4 wt% Ag alloys is shown in Fig. 12. For both Pb–1 and Pb–2.4 wt% Ag alloys, the corrosion resistance decreases with the increase in distance from the bottom of the casting. Due to this reason, it can be said that for Pb–Ag dendritic alloys, a finer dendritic array would be more appropriate in terms of corrosion behavior. This is associated with a lower current density and higher charge transfer resistance or resistance associated with absorbed intermediate species. This indicates that the growth of stable PbO₂ can be suppressed and the charge–discharge cycle increased, which corresponds to an increase in the life-cycle of the battery. It is known that fine dendritic microstructures are usually obtained in components that are manufactured by continuous casting processes.

It can be said that both the Pb–1 and 2.4 wt% Ag alloys have at the position P1 dendritic arrays three and 6.5 times finer than at P2 and P3, respectively. For the Pb–1 wt% Ag alloy, a comparison between the finer and the coarser dendritic arrays reveals that at P1 (finer λ_2 array) the dendritic spacing is 10 times smaller and the current density is 4 times lower than the corresponding values of the coarser dendritic arrays. Analyzing the finer (P1) and coarser (P3) dendritic arrays for the Pb–2.4 wt% Ag alloy, the lowest current density is also that of P1 (about 6 times lower). The experimental results of current density and impedance parameters (mainly R_1 and R_2) give indications that a slightly higher amount of silver alloying provides a better corrosion resistance, as depicted in

Table 1
Impedance parameters of examined Pb–1 wt% Ag alloy samples in a 0.5 M H₂SO₄ solution at room temperature.

Positions	P1 (10 mm)	P2 (37 mm)	P3 (65 mm)
Dendritic spacings	±8 μm	±25 μm	±46 μm
Parameters			
R_{el} (Ω cm ²)	4.5	4.4	4.1
$Z_{\text{CPE}}(1)$ (μF cm ^{−2})	391 (±5)	1592 (±110)	1440 (±98)
$Z_{\text{CPE}}(2)$ (10 ³ F cm ^{−2})	106 (±60)	5.4 (±2.5)	5.1 (±1.2)
n_1	0.72	0.64	0.64
n_2	0.84	0.81	0.66
R_1 (Ω cm ²)	344 (±6)	121 (±7)	84 (±21)
R_2 (Ω cm ²)	19 (±5)	106 (±27)	135 (±42)
χ^2	64 × 10 ^{−4}	88 × 10 ^{−4}	81 × 10 ^{−4}

Table 2
Impedance parameters of examined Pb–2.4 wt% Ag alloy samples in a 0.5 M H₂SO₄ solution at room temperature.

Positions	P1 (10 mm)	P2 (37 mm)	P3 (65 mm)
Dendritic spacings	±6 μm	±21 μm	±39 μm
Parameters			
R_{el} (Ω cm ²)	4.2	4.8	4.8
$Z_{\text{CPE}}(1)$ (μF cm ^{−2})	42.5 (±1.9)	387 (±68)	1685 (±265)
$Z_{\text{CPE}}(2)$ (10 ^{−3} F cm ^{−2})	0.29 (±0.1)	4.8 (±15)	5.3 (±0.9)
n_1	0.72	0.79	0.63
n_2	0.77	0.70	0.72
R_1 (Ω cm ²)	18 (±0.6)	38 (±9)	74 (±11)
R_2 (Ω cm ²)	552 (±6)	115 (±15)	97 (±15)
χ^2	11 × 10 ^{−4}	78 × 10 ^{−4}	84 × 10 ^{−4}

Fig. 12. Zhang and Houlachi [16] have reported a similar tendency for dilute Pb–Ag alloys. They stated that even with Pb–Ag alloys having low silver contents (0.7–1.0%) the oxygen overvoltage decreased and improved the corrosion resistance. However, the silver content of the alloy cannot be considered as the single driving-force determining the electrochemical behavior of a Pb–Ag alloy.

The experimental results of the present investigation permit to conclude that the silver content of the Pb–Ag alloy associated with the applied cooling rate during casting has a fundamental role on

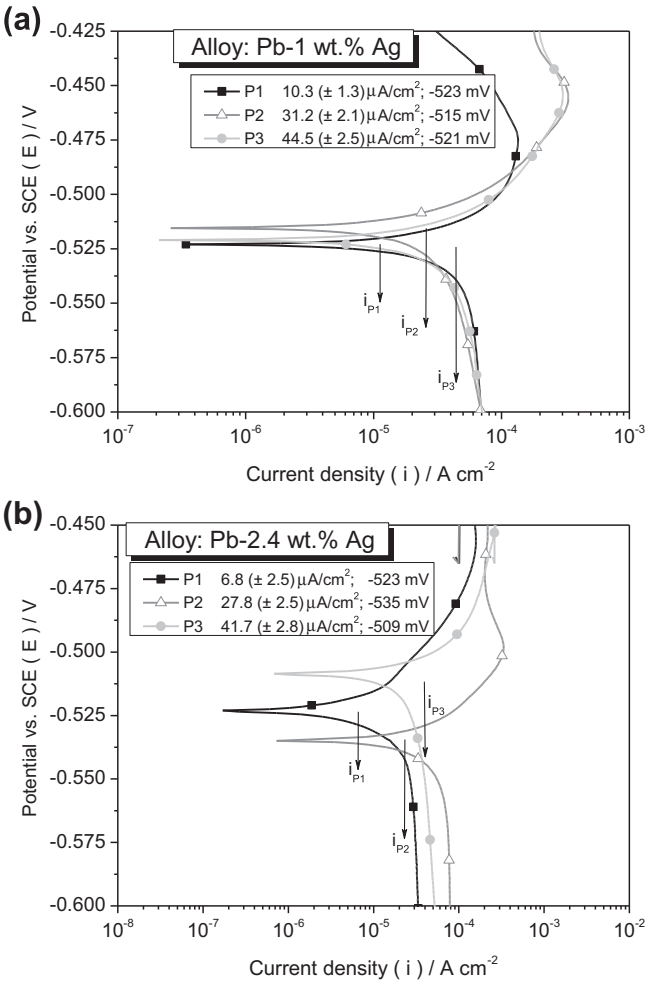


Fig. 11. Potentiodynamic polarization curves in a 0.5 M H₂SO₄ solution at 25 °C for: (a) Pb–1 wt% Ag alloy from –600 mV (SCE) to –425 mV (SCE) and (b) Pb–2.4 wt% Ag alloy from –600 mV (SCE) to –450 mV (SCE).

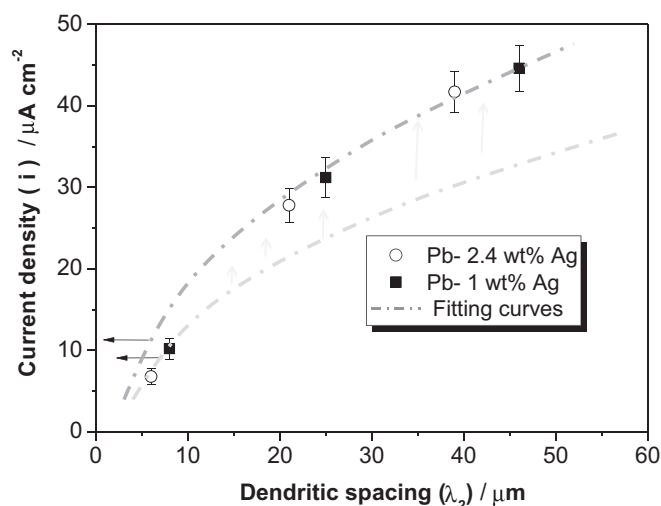


Fig. 12. Experimental current density (i_{corr}) data in a 0.5 M H_2SO_4 solution at 25 °C with secondary dendritic spacings for Pb-1 wt.% Ag and Pb-2.4 wt.% Ag alloys.

the resulting microstructure array and consequently on the electrochemical corrosion response. It was shown that the higher silver content has induced a slightly finer dendritic array when similar positions in the casting are considered (P1, P2, P3), and that the current density increases with the increase in λ_2 , as depicted in Fig. 12. However, for positions P2 and P3 (range of λ_2 between 20 and 50 μm), the current density tends to be in a similar range of results in each of these positions for both alloys. It would be expected a considerable improvement on the corrosion resistance (i.e. lower current density) for the Pb–Ag alloy with higher silver content since Ag is nobler than Pb (about 150 mV, SCE in sea-water at room temperature [28]). As aforementioned in Section 3.1, tertiary dendritic branches have been detected at positions P2 and P3 of the Pb-2.4 wt.% Ag alloy casting. For positions close to the cooled bottom of the latter alloy casting and along the entire Pb-1 wt.% Ag alloy casting the dendritic arrangement is characterized only by primary and secondary dendritic branches. The presence of tertiary branches makes the dendritic pattern more complex and permits a more homogeneous distribution of the interdendritic product throughout the microstructure. This is intimately associated with the silver content and the eutectic fraction (about 38.5% and 95.8% for the Pb-1 and Pb-2.4 wt.% Ag alloys, respectively). This has significantly increased the anodic/cathodic area ratio (Aa/Ac), which means that the Pb-matrix areas decreased and the regions with Ag-rich phase increased resulting in a more severe and drastic corrosion rate due to galvanic cell couples. Besides, it can also be considered that tertiary dendritic branches have spread the galvanic couple regions, which is intimately correlated with the anode/cathode area ratios. This explains the similar impedance and Nyquist plots for positions P2 and P3, as shown in Figs. 8(b) and 9(b). Besides, this can also explain the oscillations on the impedance resistances R_1 and R_2 (Tables 1 and 2), evidencing the predominant participation of adsorbed species when the Pb-2.4 wt.% Ag alloy is considered.

In order to determine the Aa/Ac ratio for the examined Pb–Ag alloys, the software ImageJ® was used. Some selected images of positions P1 and P3 of the Pb-1 wt.% Ag alloy samples were converted into binary images and 10 measurements of areas were carried out. It is also important to remember that the measured areas constitute about 80–90% of the binary image examined, in order to standardize the measurements and errors.

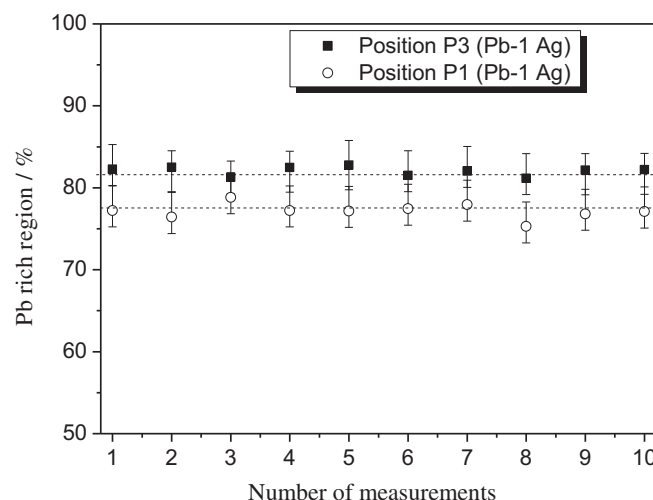


Fig. 13. Percentage of Pb-rich region in binary images of resulting microstructure of a Pb-1 wt.% Ag alloy.

The percentages of the Pb-rich matrix (less-noble area) and the interdendritic regions (nobler area) were determined, as shown in Fig. 13. It can be seen that these experimental values of the Pb-rich areas in the binary images are very similar to those determined by the Scheil's equation (f_E of 38.5% for the Pb-1 wt.% Ag alloy). Since the eutectic structure is formed by alternated lamellae of Pb-rich and Ag-rich phases, the total Pb-rich phase constitutes 80.75% (i.e. 61.5% from the Pb-rich dendritic matrix region and 19.25% from the Pb-rich lamellae in the eutectic mixture). The estimated values of these Pb-rich regions using binary images of the Pb-1 wt.% Ag alloy evidenced about 78 and 82% of these regions at positions P1 and P3, respectively. Although this difference seems to be associated with the interpretation of the black and white regions of each examined binary image, the values are quite similar and the Scheil's equation can be seen as a useful tool in the determination of anode/cathode area ratios.

The calculated Aa/Ac ratio for the Pb-1 wt.% Ag and Pb-2.4 wt.% Ag alloys are about 1:5 and 1:2, respectively. The Ag is the cathode in the anodic areas and the Pb is the anode in the cathodic sites. From these discussions, it is possible to realize that the microstructural array has a role on the corrosion current density, which is more influent than that of the silver alloying.

Considering the experimental values of i_{corr} and λ_2 in a same alloy, from the position P1 to P2 both i_{corr} and λ_2 increased about 3 times and from P2 to P3, increased 1.5 and 1.8, respectively. Although the silver content has increased about 2.5 times from one alloy to another (Aa/Ac of 1:5–1:2) the variations in i_{corr} and λ_2 from P1 to P2 and P2 to P3 have a same order of magnitude. Independently of the silver content, the corrosion rate and the scale of the dendritic array (λ_2) exhibit an evident proportionality. On the other hand, comparing these parameters of both Pb-2.4 wt.% Ag and Pb-1 wt.% Ag alloys, i.e. analyzing the silver content effect, it can be seen that the Ag content has more impact at P1 (where λ_2 is about 33% smaller for the Pb-2.4 wt.% Ag alloy and i_{corr} decreased about 52%), as shown in Fig. 14. For P2 and P3, i_{corr} decreased 12% and 7% and λ_2 19% and 18%, respectively. This means that the duplication or triplication of the Ag alloying has not the same proportional effect on the corrosion current density, but a proportional effect can be attained with the refinement of the dendritic array. However, the Aa/Ac ratio should be carefully analyzed due to the aforementioned galvanic effect between Ag-rich and Pb-rich phases. The addition of nobler elements to anode matrices with

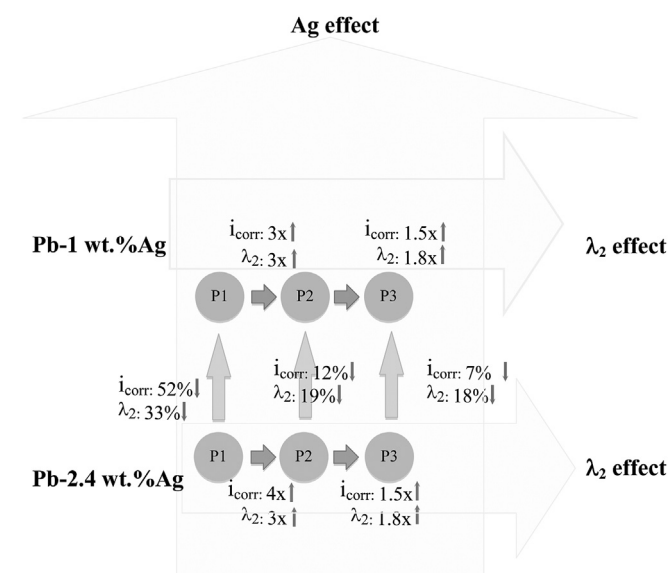


Fig. 14. Effect of both Ag content and secondary dendritic arm spacing (λ_2) on the current density (i_{corr}) for the Pb-1 wt.% Ag and Pb-2.4 wt.% Ag alloys.

fine dendritic microstructural arrays has also been reported for a number of other binary alloys, such as Pb-6.6 wt.% Sb [23,24], Al-4.5 wt.% Cu [29] and Al-Ni [30] alloys.

Considering the manufacture of Pb-acid battery components, the small Ag amount to be added to Pb or to a Pb-based alloy and the choice of an appropriate range of cooling rates that must be applied during casting, seem to be important actions to be pre-programmed in order to permit the best electrochemical response of such battery components to be attained.

It is known that both Pb-Sb and Pb-Sn alloys are widely used in a number of grid manufacturing processes. The manufacturers of battery components have focused on the decrease of battery grid weight as well on the reduction of production costs and improvements on its electrochemical behavior for both VRLA and SLI batteries. Table 3 synthesizes characteristics such as current density (i_{corr}), density and average cost of the three distinct binary Pb-based alloys having the same weight percentage of solute content (1 wt.%), i.e. Pb-Sb, Pb-Sn and Pb-Ag alloys. Since Ag is a very expensive metal (between US\$ 800 and 1000 per kg), the Pb-Ag alloy is the most expensive material for battery components (about ten times higher than those of the other alloys). Although both Sb (6.7 g cm^{-3}) and Sn (7.3 g cm^{-3}) are slightly lighter than Ag (10.5 g cm^{-3}), its small weight percentage addition (1 wt.%) to Pb (11.34 g cm^{-3}) gives alloys of similar final densities.

From the experimental results for i_{corr} obtained in this investigation, compared with those previously reported for as-cast Pb-Sb [17,18,23,24] and Pb-Sn [19–22] alloys, which have been correlated with finer (cooling rates $>10 \text{ }^\circ\text{C s}^{-1}$) and coarser (cooling rate

$<1 \text{ }^\circ\text{C s}^{-1}$) microstructure arrays, two assertions can be drawn. Firstly, when a fine microstructural array is obtained, the lowest corrosion current density (of about 3–5 times lower than those of Pb-Sb and Pb-Sn alloys) is that of the Pb-Ag alloy followed by Pb-Sb and Pb-Sn alloys. Secondly, when considering a coarser microstructure, the lowest i_{corr} is depicted by the Pb-Sn alloy followed by the Pb-Sb and the Pb-Ag alloy, which exhibits an i_{corr} about 4 times higher than these two other alloys. Although some previous studies have stated that the addition of silver to Pb or Pb-based alloys can increase the charge-discharge cycle, electrochemical activity, and as consequence improve the corrosion resistance and the life-cycle of lead-acid battery components, this investigation provides complementary information concerning the attention that should be taken on the preprogramming of the casting cooling rate (high or low) and of the resulting microstructure array (fine or coarse).

4. Conclusions

From the present experimental results concerning the microstructural array, impedance parameters, potentiodynamic polarization curves and equivalent circuit analysis, it can be concluded that the microstructural array of Pb-Ag alloys, characterized by secondary and tertiary dendrite branches, has a role on the corrosion current density, which is more significant than that of the silver alloying.

Tertiary dendritic branches have been detected along the Pb-2.4 wt.% Ag alloy casting, while for the entire Pb-1 wt.% Ag alloy casting the dendritic arrangement was shown to be characterized only by primary and secondary dendritic branches. The presence of tertiary branches makes the dendritic pattern more complex and permits a more homogeneous distribution of the interdendritic product throughout the microstructure. This associated with the anode/cathode area ratio has severely accelerated the corrosion rate caused by the formation of galvanic couples. Besides, it was also found that the Ag content has an important role on the participation of adsorbed intermediate species (values of impedance parameters: R_2 and R_1) in the electrochemical behavior of the Pb-2.4 wt.% Ag alloy, when compared with that of the Pb-1 wt.% Ag alloy.

It was also found that the scale of the dendritic microstructure provokes a proportional effect on the corrosion current density, i.e. when λ_2 experiences a decrease of 3 times there is a corresponding decrease in i_{corr} of about 3 times. On the other hand, the Ag content of the alloy should be meticulously analyzed and associated with the Aa/Ag ratio and the magnitude of λ_2 .

A comparative analysis carried out with Pb-Sb, Pb-Sn, and Pb-Ag alloys having a same weight percentage of solute (i.e. 1 wt.%) has shown that the lowest i_{corr} is that of Pb-Ag alloy for a fine microstructural array. Although the silver price represents a disadvantage and considerably increases the final cost of Pb-Ag alloys, these alloys are qualified as alternative materials of choice for lead-acid battery components. This choice has to be associated with manufacturing casting systems that provide high cooling rates, e.g. permanent mold casting or continuous casting.

Acknowledgments

The authors acknowledge the financial support provided by CNPq (The Brazilian Research Council), FAEPEX-UNICAMP, and FAPESP.

References

- [1] J.A. Bialacki, N.A. Hampson, F. Wilson, J. Appl. Electrochem. 15 (1985) 99–105.

Table 3

Comparative values of the cost per kilogram, density and current density for Pb-1 wt.% Sb, Pb-1 wt.% Sn and Pb-1 wt.% Ag alloys.

Material	Average cost (\$US kg ⁻¹) ^a	Density (g cm ⁻³) ^a	i_{corr}^b ($\mu\text{m cm}^{-2}$)
Pb-1 wt.% Sb	1.4–1.6	11.29	33
Pb-1 wt.% Sn	1.3–1.5	11.30	46
Pb-1 wt.% Ag	10–15	11.33	10

^a Values estimated from the individual prices (based on Brazilian market) and densities.

^b Average and approximately values.

- [2] R.L. Cui, S.G. Wu, *J. Power Sources* 46 (1993) 327–333.
- [3] R.D. Prengaman, *J. Power Sources* 67 (1997) 267–278.
- [4] R.D. Prengaman, *J. Power Sources* 95 (2001) 224–233.
- [5] T. Hirasawa, K. Sasaki, M. Taguchi, H. Kaneko, *J. Power Sources* 85 (2000) 44–48.
- [6] B.K. Mahato, J.L. Strebe, D.F. Wilkinson, K.R. Bullock, *J. Electrochem. Soc.* 132 (1985) 19–23.
- [7] B. Rezaei, S. Damiri, *J. Solid State Electrochem.* 9 (2005) 590–594.
- [8] J. Furukawa, Y. Nehyo, S. Shiga, *J. Power Sources* 133 (2004) 25–31.
- [9] D. Slavkov, B.S. Haran, B.N. Popov, F. Fleming, *J. Power Sources* 112 (2002) 199–208.
- [10] Y.B. Zhou, C.X. Yang, W.F. Zhou, H.T. Liu, *J. Alloys Compd.* 365 (2004) 108–111.
- [11] H.T. Liu, J. Yang, H.H. Liang, J.H. Zhuang, W.F. Zhou, *J. Power Sources* 93 (2001) 230–233.
- [12] E. Bashtavelova, A. Winsel, *J. Power Sources* 67 (1997) 93–103.
- [13] W.X. Guo, D. Shu, H.Y. Chen, A.J. Li, H. Wang, G.M. Xiao, C.L. Dou, S.G. Peng, W.W. Wei, W. Zhang, H.W. Zhou, S. Chen, *J. Alloys Compd.* 475 (2009) 102–109.
- [14] P. Yu, T.J. O'Keefe, *J. Electrochem. Soc.* 146 (1999) 1361–1369.
- [15] M. Stevenson, in: C.K. Dyer, P.T. Moseley, Z. Ogumi, D. Rand, D. Scrosati (Eds.), *Encyclopedia of Electrochemical Power Sources, Recycling, Lead-Acid Batteries: Overview*, vol. 4, Elsevier, Amsterdam, 2009, ISBN 978-0-444-52093-7, pp. 165–178.
- [16] W. Zhang, G. Houlachi, *Hydrometallurgy* 104 (2010) 129–135.
- [17] D.M. Rosa, J.E. Spinelli, W.R. Osório, A. Garcia, *J. Power Sources* 162 (2006) 696–705.
- [18] W.R. Osório, D.M. Rosa, A. Garcia, *J. Power Sources* 175 (2008) 595–603.
- [19] L.C. Peixoto, W.R. Osório, A. Garcia, *J. Power Sources* 192 (2009) 724–729.
- [20] W.R. Osório, L.C. Peixoto, A. Garcia, *J. Power Sources* 194 (2009) 1120–1127.
- [21] W.R. Osório, L.C. Peixoto, A. Garcia, *J. Power Sources* 195 (2010) 1726–1730.
- [22] L.C. Peixoto, W.R. Osório, A. Garcia, *J. Power Sources* 195 (2010) 621–630.
- [23] W.R. Osório, D.M. Rosa, L.C. Peixoto, A. Garcia, *J. Power Sources* 196 (2011) 6567–6572.
- [24] W.R. Osório, E.S. Freitas, L.C. Peixoto, J.E. Spinelli, A. Garcia, *J. Power Sources* 207 (2012) 183–190.
- [25] W. Kurz, D.J. Fisher, *Fundamentals of Solidification*, Trans. Tech. Publications, Switzerland, 1992.
- [26] S. Gudic, J. Radosevic, M. Kliskic, *Electrochim. Acta* 47 (2002) 3009–3016.
- [27] M. Aziz-Kerrzo, K.G. Conroy, A.M. Fenelon, S.T. Farrell, C.B. Breslin, *Bio-materials* 22 (2001) 1531–1539.
- [28] Mil-Std 889B – Military Standard: Dissimilar Metals, Notice 3 (1993).
- [29] W.R. Osório, J.E. Spinelli, I.L. Ferreira, A. Garcia, *Electrochim. Acta* 52 (2007) 3265–3273.
- [30] W.R. Osório, L.C. Peixoto, M.V. Canté, A. Garcia, *Electrochim. Acta* 55 (2010) 4078–4085.